IET Science, Measurement & Technology

Research Article

Highly efficient approach to the simulation of variable-speed induction motor drives

ISSN 1751-8822
Received on 4th April 2017
Revised 24th April 2017
Accepted on 10th May 2017
E-First on 18th July 2017
doi: 10.1049/iet-smt.2017.0152
www.ietdl.org

Georg von Pfingsten[1] ✉, *Kay Hameyer*[1]

[1] *Institute of Electrical Machines, RWTH Aachen University, Schinkelstr. 4, Aachen, Germany*

✉ *E-mail: georg.vonpfingsten@iem.rwth-aachen.de*

Abstract: Loss modelling for induction machines operated as variable speed drives (VSD) is indispensable for designing highly utilised traction machines. Accurate loss modelling can be performed using finite-element analysis (FEA). Since VSD have to deliver torque at different values of mechanical speed, the torque-speed operating points are sought. For those torque-speed operating points, the drive should be operated in the highest efficiency points. Finding these points from transient FEA requires the simulation of several ten to hundreds operating points in terms of stator current and rotor fundamental frequency. For that reasons, local loss modelling using FEA is very time consuming. This study will present a hybrid simulation approach coupling numerical and analytical models to reduce simulation time for simulation of the torque-speed operating points. The simulation approach takes into account the inverter voltage and current limitations and finds the highest efficiency operating point for every torque-speed operating point.

Nomenclature

$\hat{x}$	peak value
$\boldsymbol{x}$	vector
x'	transformed value
$\underline{x}$	complex number
1	fundamental component
1	stator
2	rotor
bar	rotor bars
Cu	copper
Fe	soft magnetic material
M	magnetisation
min	minimum
max	maximum
nl	no-load condition
req	requested operating point
s	slot
σ	stray flux
A	area, m^2
A	magnetic vector potential solution, Vs/m
f	frequency, Hz
i	element number, dimensionless
I	electrical current, A
J	electrical current density, A/mm^2
k	loss increase due to harmonics
k	saturation state, dimensionless
k_c	Carter's factor, dimensionless
K	number of saturation states, dimensionless
l	active length, m
L	inductance, H
$\boldsymbol{L}$	inductance matrix, H
m	natural number, dimensionless
n	speed, rpm
op	operating point in terms of torque and speed, dimensionless
P	power, W
R	resistance, Ω
s	slip, dimensionless
T	time constant, s
T	torque, Nm
ts	time step, dimensionless
U	voltage, V
w	width, mm
x, y, z	Cartesian coordinates, mm
δ	length of air gap, mm
Δ	error, dimensionless
γ	auxiliary number, dimensionless
ω	angular frequency, rad/s
ψ	flux linkage, Vs
σ	electrical conductivity, $1/(\Omega m)$
τ	pitch, mm

1 Introduction

Electric machines for mobile traction applications, such as propulsion of electric and hybrid electric vehicles, have to meet high requirements in terms of power density, torque density and efficiency [1–3]. These requirements lead to increased operating speeds and fundamental operating frequencies much higher than of standard 50/60 Hz grid-operated machines. With increased speed and fundamental operating frequency, the share of the iron losses on the total losses increases. Hence, these high-power density drives lead to the need for loss models that accurately model the losses at high fundamental operating frequencies.

Modelling the losses of induction machines (IM) operated as variable speed drives (VSD) can be performed in different levels of detail. Loss models based on fundamental wave air gap models cannot directly consider iron losses from harmonics or local distortion of the magnetic flux. When tuned to machine measurements, these fundamental models can still be accurate in certain operating regions. Since fundamental models neglect several loss effects that are important for VSD, the accuracy of the loss modelling is constrained to a small area around the measured operating points.

Harmonic analytic models can be used to model additional Ohmic losses from harmonics. These models, such as [4, 5], rely on conformal mapping and therefore cannot model the local distribution of magnetic flux density in the soft magnetic cores. In [6], it is shown that for highly utilised traction drives, the study of saturation significantly contributes to IM design. Hence, models that do not take saturation into account are not well suited for traction drive loss modelling. Finite-element analysis (FEA) can be used to overcome these limitations from analytical models.

In this paper, the loss modelling approach from [7] based on transient non-linear 2D FEA simulations is enhanced to a hybrid

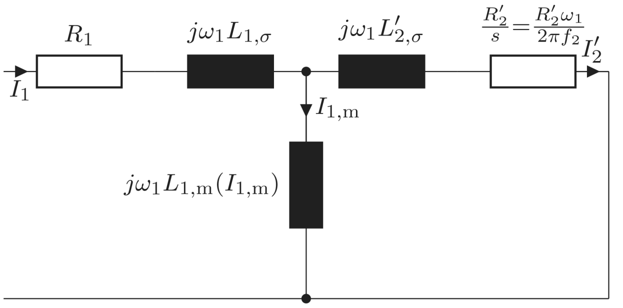

Fig. 1 *T-equivalent circuit of an IM*

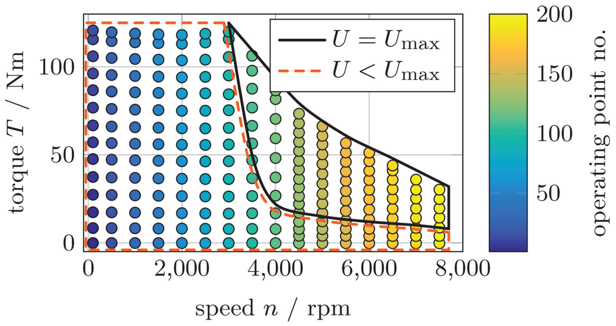

Fig. 2 *Measured operating points across the* $T - n$ *plane*

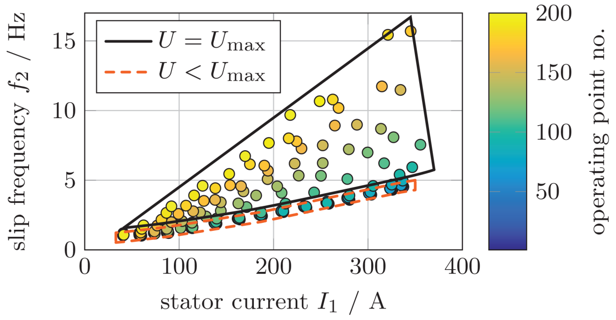

Fig. 3 *Measured operating points across the* $I_1 - f_2$ *plane*

simulation approach to reduce computational effort and directly simulate the torque–speed operating points. IM can reach a torque–speed operating point with different levels of flux linkage. Choosing the right value of flux linkage reduces the losses. The torque–speed operating points with minimal losses in [7] are found in the post processing of a variation of FEA simulations in the stator current and rotor frequency domain. These variations require a large computational effort of 1000–5000 core hours for the calculation of an entire torque–speed map. A hybrid simulation model which reduces this effort is sought and discussed in this paper.

In Section 2, the description of the magnetic circuit in terms of the stator current and rotor frequency plane is outlined. The extraction method of the inductance matrix from static FEA is verified in Section 3. Furthermore, the two hybrid simulation models are depicted. Section 4 gives an exemplary application of the hybrid simulation models to study the influence of stator and rotor slot opening shapes on the maximum machine power in dependency of machine speed. The influence of the slot opening shapes on the losses is derived. The paper concludes with a discussion of the results and possible future research topics.

2 Magnetic circuit in terms of the $I_1 - f_2$ plane

The most common way for describing the magnetic circuit of IM is the single-phase T-equivalent circuit (Fig. 1). The apparent rotor resistance R'_2/s from this equivalent circuit can be transformed into:

$$\frac{R'_2}{s} = \frac{R'_2 \times f_1}{f_2} = R'_2 \times \frac{\omega_1}{2\pi f_2}. \tag{1}$$

Hence, the apparent rotor resistance R'_2/s (1) and the three reactances in the T-equivalent circuit (Fig. 1) are proportional to ω_1. The concentrated stator resistance is the only component of the T-equivalent circuit, which is not linear dependent on ω_1. Since the stator current in the simulation is considered as an ideal current source, the stator resistance does not influence the allocation of the machine currents. The voltage drop on the stator resistance is added to the terminal voltage from the simulation in the post processing of the FEA solutions.

From the T-equivalent circuit, the allocation of the stator current I_1 into the rotor current I'_2 and the magnetising current $I_{1,\mathrm{m}}$ is solved easily:

$$\begin{aligned}\underline{I}_{1,\mathrm{m}} &= \frac{\mathrm{j}\omega_1 L'_{2,\sigma} + (R'_2\omega_1/2\pi f_2)}{\mathrm{j}\omega_1 L'_{2,\sigma} + (R'_2\omega_1/2\pi f_2) + \mathrm{j}\omega_1 L_{1,\mathrm{m}}} \times \underline{I}_1 \\ &= \frac{\mathrm{j}L'_{2,\sigma} + (R'_2/2\pi f_2)}{\mathrm{j}L'_{2,\sigma} + (R'_2/2\pi f_2) + \mathrm{j}L_{1,\mathrm{m}}} \times \underline{I}_1,\end{aligned} \tag{2}$$

$$\underline{I}'_2 = \frac{\mathrm{j}L_{1,\mathrm{m}}}{\mathrm{j}L'_{2,\sigma} + (R'_2/2\pi f_2) + \mathrm{j}L_{1,\mathrm{m}}} \times \underline{I}_1. \tag{3}$$

Equations (2) and (3) show that the allocation of the stator current $\underline{I}_1$ into the rotor current I'_2 and the magnetising current $I_{1,\mathrm{m}}$ is independent on ω_1. In fact, the allocation of the currents only depends on the state of saturation, i.e. the value of $L_{1,\mathrm{m}}$ and the frequency of the rotor currents f_2. Hence, the magnetic state of the machine is uniquely described by a combination of $\underline{I}_1$ and f_2. Thus, the operating points in terms of torque T and speed n are modelled using the $\underline{I}_1 - f_2$ plane.

Fig. 2 shows the measured operating points of a 40 kW (peak) squirrel cage IM. These $T - n$ operating points are transferred to the $\underline{I}_1 - f_2$ plane in Fig. 3. The number of the operating point is individually indicated by its colour/greyscale. The operating points of the machine operated at the maximum efficiency for every torque and speed correspond to combinations of $\underline{I}_1 - f_2$ within a small region. The operating points below the voltage limitation of the inverter are found on only one trajectory, whereas the operating points at the voltage limit are found in a triangular region at higher values of f_2 (Fig. 3).

As described in [7, 8], the torque-speed operating points can be derived from simulations in the $\underline{I}_1 - f_2$ plane. However, several ten to hundreds of transient FEA simulations have to be conducted to do so. Since several hundred simulation time steps have to be calculated for every $\underline{I}_1 - f_2$ combination before reaching steady state, a total computation time of several thousand core hours for the torque-speed map of an IM is consequential.

To reduce this very high computational effort, two hybrid simulation models are introduced in the following section.

3 Hybrid simulation model for reduced computational effort

Two variants of a hybrid simulation model, which are suitable for different purposes, are described. The first variant is the *pre-calculation of steady state* of a transient FEA simulation. The analytic fundamental wave formulation is coupled with a static FEA simulation to cut short the transient build-up of the flux linkages. The first hybrid model requires that the operating point in terms of stator current density $\hat{J}_1$ and f_2 is known. The second variant *calculation of a single loss minimal torque-speed operating point* removes this requirement.

3.1 Extraction of the inductances from static no-load FEA simulations

Fig. 4 shows the labels of the stator and rotor conductors. From each label i to another label j, an inductance value L_{ij} is extracted as described in [9]. From these values L_{ij}, the full inductance matrix $\boldsymbol{L}$ is formed.

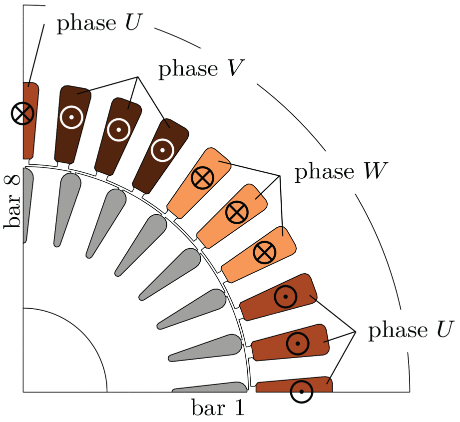

Fig. 4 *Labels of quarter model of the studied IM*

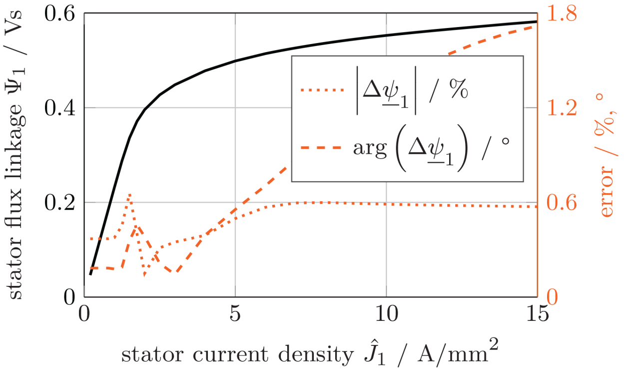

Fig. 5 *Stator flux linkage from static no-load FEA versus stator flux linkage from transient FEA*

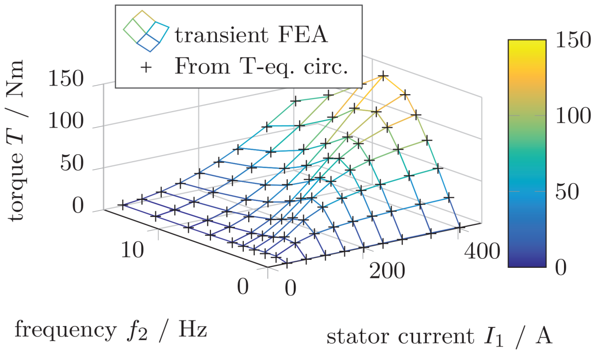

Fig. 6 *Torque directly from FEA and from T-equivalent circuit*

The matrix $\boldsymbol{L}$ fully describes the relationship between the current vectors of the stator $\boldsymbol{I}_1$ and rotor $\boldsymbol{I}_2$ currents and the corresponding flux linkage vectors $\boldsymbol{\psi}_1$ and $\boldsymbol{\psi}_2$ (4). The matrix $\boldsymbol{L}$ is subdivided in the mutual inductance matrices $\boldsymbol{L}_{12}$ and $\boldsymbol{L}_{21}$ and the self-inductance matrices $\boldsymbol{L}_{11}$ and $\boldsymbol{L}_{22}$.

$$\begin{bmatrix}\boldsymbol{\psi}_1\\ \boldsymbol{\psi}_2\end{bmatrix} = \boldsymbol{L}\begin{bmatrix}\boldsymbol{I}_1\\ \boldsymbol{I}_2\end{bmatrix} = \begin{pmatrix}\boldsymbol{L}_{11} & \boldsymbol{L}_{12}\\ \boldsymbol{L}_{21} & \boldsymbol{L}_{22}\end{pmatrix}\begin{bmatrix}\boldsymbol{I}_1\\ \boldsymbol{I}_2\end{bmatrix} \quad (4)$$

The stator flux linkage vector $\boldsymbol{\psi}_1(t,\hat{J}_1)$ is evaluated for different stator excitation current density values $\hat{J}_1$ and different simulation time steps ts at no-load condition ($f_2 = 0$). The space vector $\boldsymbol{\psi}_1$ is transformed into a complex vector $\underline{\boldsymbol{\psi}}_1$ (5). The maximum difference in length and in terms of angular position is computed according to (6) and (7). Fig. 5 shows the error of the stator flux linkage in dependency of saturation, i.e. in dependency of $\hat{J}_1$. The maximum error in vector length is 0.66%. The maximum error in angular position of the stator flux linkage is 1.72°. These results show that the inductance matrix can describe the magnetic circuit of the IM with good accuracy. Therefore, the inductance matrix $\boldsymbol{L}$ extracted using the method from [9] is suitable to model the magnetic circuit.

$$\underline{\boldsymbol{\psi}}_1 = \boldsymbol{\psi}_1 \times \begin{bmatrix}1\\ \mathrm{e}^{\mathrm{j}120^\circ}\\ \mathrm{e}^{\mathrm{j}240^\circ}\end{bmatrix} \quad (5)$$

$$\left|\Delta\underline{\boldsymbol{\psi}}_1(\hat{J}_1)\right| = 1 - \frac{\min_{\mathrm{ts}}\left(\left|\underline{\boldsymbol{\psi}}_1(\mathrm{ts},\hat{J}_1)\right|\right)}{\max_{\mathrm{ts}}\left(\left|\underline{\boldsymbol{\psi}}_1(\mathrm{ts},\hat{J}_1)\right|\right)} \quad (6)$$

$$\begin{aligned}\arg\left(\Delta\underline{\boldsymbol{\psi}}_1(\hat{J}_1)\right) = &\max_{\mathrm{ts}}\left(\arg\left(\underline{\boldsymbol{\psi}}_1(\mathrm{ts},\hat{J}_1)\right)\right)\\ &-\min_{\mathrm{ts}}\left(\arg\left(\underline{\boldsymbol{\psi}}_1(\mathrm{ts},\hat{J}_1)\right)\right)\end{aligned} \quad (7)$$

Fig. 6 shows the torque from transient FEA simulations after reaching steady state (mesh plot) in dependency of f_2 and I_1. A fundamental wave T-equivalent circuit with constant stray flux parameters $L_{1,\sigma}$, $L'_{2,\sigma}$, constant rotor resistance R'_2 and saturation-dependent main inductance $L_{1,\mathrm{m}}(I_{1,\mathrm{m}})$ is identified using the simulated torque values in dependency of $\underline{I}_1$ and f_2. The calculated values of stator flux linkage and torque of the machine using this identified T-equivalent circuit are also plotted in Fig. 6 (black crosses). A difference of < 2.23 Nm (1.5%) and 4.1 mVs (2.6%) between the FEA results and the identified T-equivalent circuit is found. Hence, the conventional equivalent circuit with concentrated parameters is well suited to simulate operating points in terms of torque and speed.

Since the concentrated values of the magnetic circuit have proved to be sufficiently accurate to model torque and flux linkage, two simulation schemes are created which couple static and transient FEA simulations with analytic formula.

3.2 Pre-calculation of steady state

This first simulation scheme derives the saturation state of the magnetic circuit by solving the analytic formulation for the rotor currents calculated from the concentrated parameters extracted from static no-load simulations. The simulation scheme is shown in Fig. 7.

First, one time step ts = 0 of non-linear no-load static FEA simulations is conducted. The stator current density $\hat{J}_1$ is the only excitation in this first simulation. The small letter k consecutively denotes the saturation state by natural numbers, with smaller k meaning lower flux linkage and higher k meaning higher flux linkage. The capital letter K denotes the highest simulated saturation state with the highest stator current density $\hat{J}_{1,\max}$. $\hat{J}_1$ is varied between zero $\hat{J}_1(k=1)=0$ and the maximum current density $\hat{J}_1(k=K)=\hat{J}_{1,\max}$. By doing so, various saturation states between unsaturated and maximum saturation are simulated. For each of the values of $\hat{J}_1(k)$, the full non-linear inductance matrix $\boldsymbol{L}(k)$ is extracted.

The static no-load (index nl) simulation and extraction of $\boldsymbol{L}$ less than 1 core minute per current density. In contrast, for a transient simulation to reach the steady state, several hundred simulation time steps, i.e. several core hours are necessary. Since the static simulations can be independently calculated, parallelisation on multiple CPU cores is possible. For the exemplary machine, approximately ten core minutes on a machine equipped with one Intel Core i5-4570S, 2.9 GHz and 16 GB memory are necessary for the characterisation of the non-linear magnetisation behaviour in $K = 23$ saturation states.

From the extracted matrix $\boldsymbol{L}_{21}(k)$ and $\boldsymbol{L}_{22}(k)$, the rotor current vector $\boldsymbol{I}_2(k)$ is calculated according to the analytic (8) for every saturation state k. Fig. 8*a* depicts the effective rotor current $\boldsymbol{I}_2$ for different values of stator current density $\hat{J}_1$ in dependency of the saturation state $\hat{J}(k)$ at a frequency of $f_2 = 5$ Hz. The stator current vector $\boldsymbol{I}_1$ and the saturation-dependent rotor current vector $\boldsymbol{I}_2(k)$ are

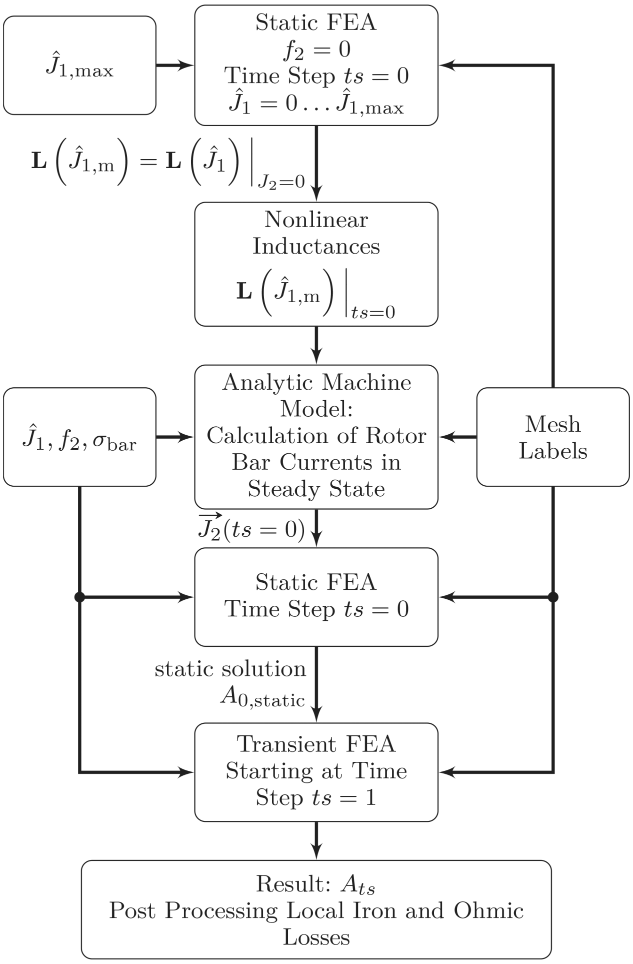

Fig. 7 *Scheme for hybrid simulation model predicting the starting value of rotor flux*

used to calculate the stator flux linkage vector $\boldsymbol{\psi}_1(k)$ for every saturation state k according to (9). The rotor flux linkage vector $\boldsymbol{\psi}_2(k)$ is calculated according to (10). The no-load stator flux linkage, i.e. flux linkage at zero rotor current, is calculated according to (11). The length of the flux linkage $\boldsymbol{\psi}_1(k)$ and $\boldsymbol{\psi}_{1,\mathrm{nl}}(k)$ is calculated according to (14) and (15) for every saturation state k.

Fig. 8*b* shows the length of the computed stator flux linkage $\boldsymbol{\psi}_1(k)$ and of $\boldsymbol{\psi}_{1,\mathrm{nl}}(k)$ calculated according to (14) and (15) versus the stator current density $\hat{J}_1$. The point where the length of the stator flux linkage vectors is equal describes the valid saturation state. These points are marked with black crosses in Fig. 8*b*. In each point, the equivalent stator no-load current I_0 is interpolated according to (12) and (13). The value of $\boldsymbol{I}_2$ for this point is also found by numerical interpolation. The interpolated value of $\boldsymbol{I}_2$ is used as static excitation for the FE model. From the static excitation of stator and rotor current, the magnetic vector potential $A_{0,\mathrm{static}}$ in the first simulation time step is calculated. For the following, second simulation time step, the vector potential $A_{0,\mathrm{static}}$ is used as previous solution. By applying this procedure, the number of required simulation time steps for the transient build-up of the rotor flux linkage can be drastically reduced

$$\begin{aligned}\boldsymbol{I}_2(k) &= \mathrm{inv}(-\mathrm{j} \times \omega_2 \times \boldsymbol{L}_{22}(k) + \boldsymbol{R}_2)\\ &\quad \times (\mathrm{j} \times \omega_2 \boldsymbol{L}_{21}(k) \times \boldsymbol{I}_1)\end{aligned} \tag{8}$$

$$\boldsymbol{\psi}_1(k) = \boldsymbol{L}_{11}(k) \times \boldsymbol{I}_1 + \boldsymbol{L}_{12}(k) \times \boldsymbol{I}_2(k) \tag{9}$$

$$\boldsymbol{\psi}_2(k) = \boldsymbol{L}_{21}(k) \times \boldsymbol{I}_1 + \boldsymbol{L}_{22}(k) \times \boldsymbol{I}_2(k) \tag{10}$$

$$\boldsymbol{\psi}_{1,\mathrm{nl}}(k) = \boldsymbol{L}_{11}(k) \times \boldsymbol{I}_{1,\mathrm{nl}}(k) \tag{11}$$

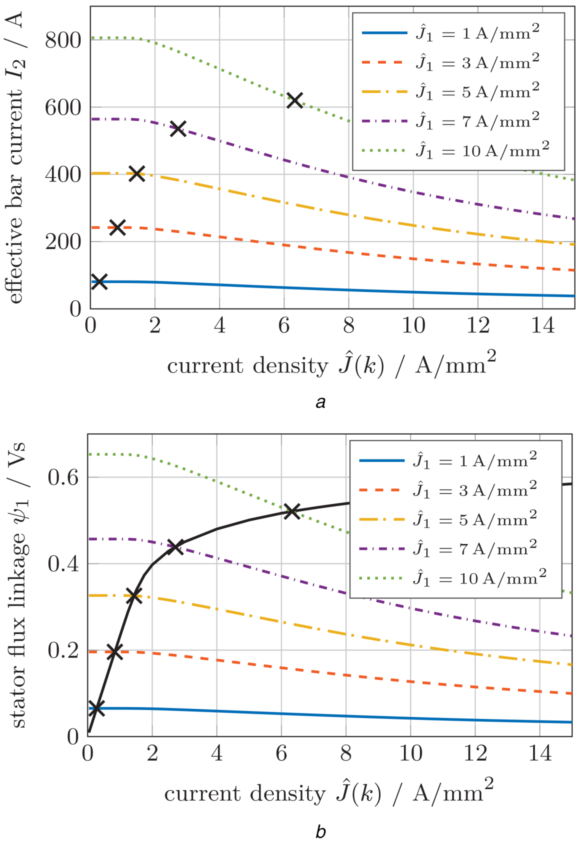

a

b

Fig. 8 *Interpolation of saturation state from lumped parameter matrix* **L** *($f_2 = 5\,\mathrm{Hz}$)*
(a) Rotor current, ***(b)*** Stator flux linkage

$$\begin{aligned}0 &= m \times \boldsymbol{\psi}_1(k) + (m-1) \times \boldsymbol{\psi}_1(k+1)\\ &\quad - m \times \boldsymbol{\psi}_{1,\mathrm{nl}}(k) - (m-1) \times \boldsymbol{\psi}_{1,\mathrm{nl}}(k+1)\\ &\quad , \quad \text{with } k = 0, 1, \ldots, K-1 \text{ and } m = 0, \ldots, 1\end{aligned} \tag{12}$$

$$I_0 = A_{\mathrm{s},1}/\sqrt{2} \times \left(m \times \hat{J}_1(k) + (m-1) \times \hat{J}_1(k+1)\right) \tag{13}$$

$$\boldsymbol{\psi}_1\left(\hat{J}_1(k)\right) = \sqrt{\frac{1}{3} \times \left(\underline{\boldsymbol{\psi}}_{1,1}^2\left(\hat{J}_1(k)\right) + \underline{\boldsymbol{\psi}}_{1,2}^2\left(\hat{J}_1(k)\right) + \underline{\boldsymbol{\psi}}_{1,3}^2\left(\hat{J}_1(k)\right)\right)} \tag{14}$$

$$\begin{aligned}&\boldsymbol{\psi}_{1,\mathrm{nl}}\left(\hat{J}_1(k)\right)\\ &= \sqrt{\frac{1}{3} \times \left(\underline{\boldsymbol{\psi}}_{1,\mathrm{nl},1}^2\left(\hat{J}_1(k)\right) + \underline{\boldsymbol{\psi}}_{1,\mathrm{nl},2}^2\left(\hat{J}_1(k)\right) + \underline{\boldsymbol{\psi}}_{1,\mathrm{nl},3}^2\left(\hat{J}_1(k)\right)\right)}\end{aligned} \tag{15}$$

The benefit of the proposed simulation scheme (Fig. 7) for the combination of analytical model and transient FEA simulation is best seen when analysing the rotor flux linkage trajectory with and without application of the simulation scheme (Fig. 9). The operating point shown in Fig. 9 is defined by a stator current density $\hat{J}_1 = 5\,\mathrm{A/mm^2}$ and slip frequency $f_2 = 15\,\mathrm{Hz}$. Figs. 9*a* and *b* show the trajectory of the rotor flux linkage vectors in dependency of the simulation time step ts with a duration of $\Delta_{\mathrm{ts}} = 1\,\mathrm{ms}$ for each step. The information of ts is represented by the colour/greyscale of the trajectories. When using the standard transient FEA formulation with zero flux linkage starting condition and the stator current density $\hat{J}_1$ as only excitation of the model, the rotor flux linkage takes several hundred simulation time steps to reach steady state (Figs. 9*a* and *c*). At $ts = 12$, the absolute value of the rotor flux linkage reaches the value in steady state (Figs. 9*a* and *c*) and shoots over value of the rotor flux linkage in steady state. For the FEA simulation with analytical starting condition, <5% error in the rotor flux vector length is achieved instantly after the first simulation step, whereas for the transient FEA simulation with zero flux linkage starting condition at $ts = 307$, <5% error are

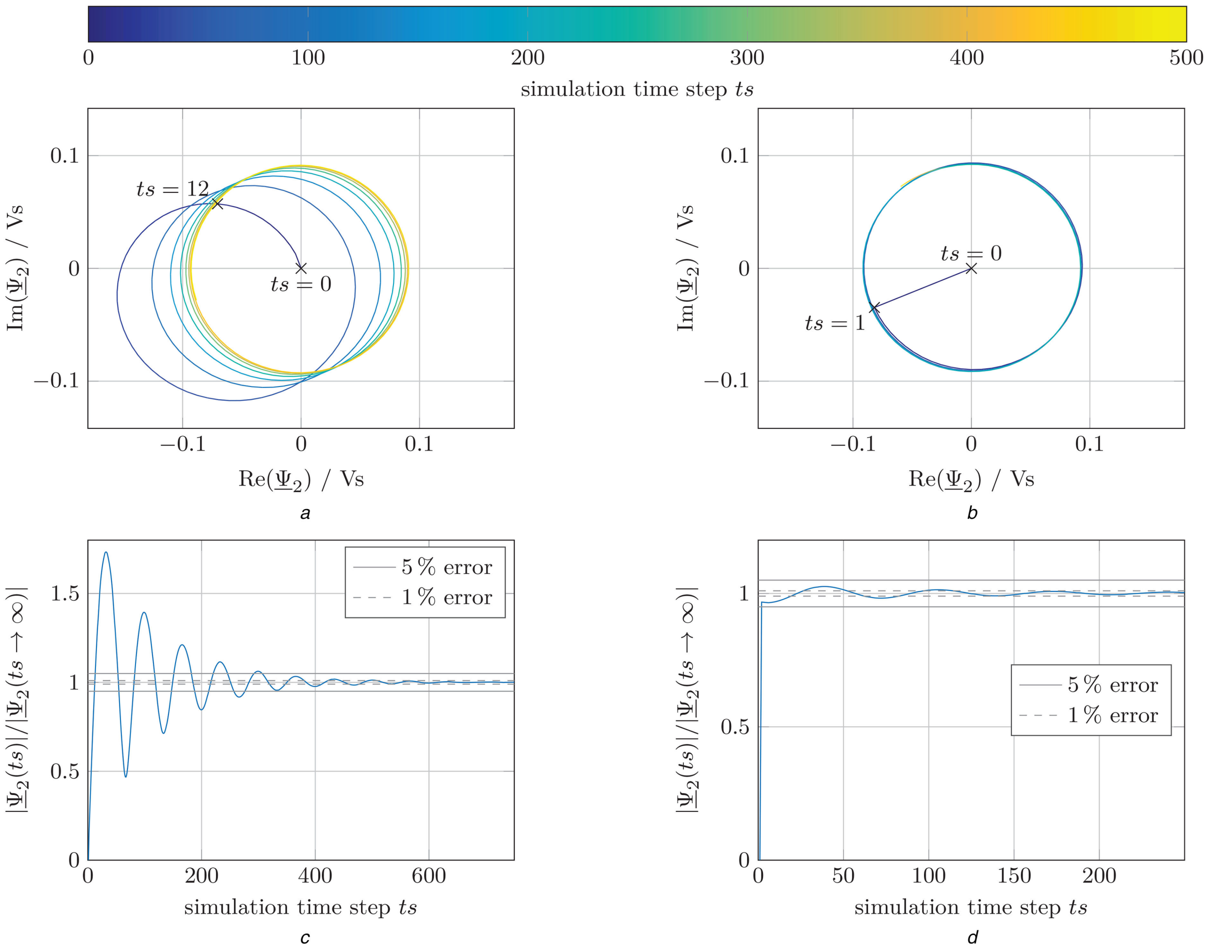

a

b

c

d

Fig. 9 *Rotor flux linkage vector in transient simulation ($\hat{J}_1 = 5\,\mathrm{A/mm^2}$, $f_2 = 15\,\mathrm{Hz}$) in dependency of the simulation time step ts. The colour/greyscale of the rotor flux linkage trajectories (a) and (b) refer to the simulation time step* ts *(colour bar on top)*

(a) Zero flux starting condition, ***(b)*** With analytical starting condition, ***(c)*** Zero flux starting condition, ***(d)*** With analytical starting condition

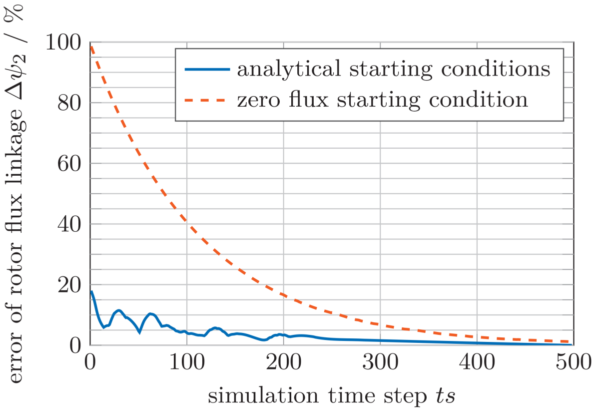

Fig. 10 *Maximum relative error $\Delta\boldsymbol{\psi}_2$ according to (16) for zero flux starting condition and for hybrid simulation model*

reached. An error of <1% is reached at $ts = 115$ and 510 correspondingly.

To show that the simulation scheme drastically reduces the simulation time for transient build-up of the flux linkages not only in one, but all relevant operating points, the maximum flux error is calculated for different combinations of $\hat{J}_1$ and f_2. The maximum relative error $\Delta\boldsymbol{\psi}_2$ of the rotor flux vector length compared with the flux vector length in steady state for all combinations of $\hat{J}_1 = 1\,\mathrm{A/mm^2}, \ldots, 10\,\mathrm{A/mm^2}$ and $f_2 = 0\,\mathrm{Hz}, \ldots, 15\,\mathrm{Hz}$ is used as quality function:

$$\Delta\boldsymbol{\psi}_2(\mathrm{ts}) = \max_{f_2, \hat{J}_1}\left(\frac{\big||\boldsymbol{\psi}_2|(\mathrm{ts}) - |\boldsymbol{\psi}_2|(\mathrm{ts} \to \infty)\big|}{|\boldsymbol{\psi}_2|(\mathrm{ts} \to \infty)}\right). \tag{16}$$

The smaller $\Delta\boldsymbol{\psi}_2$ becomes, the closer the rotor flux linkages for all operating points is to steady state. Fig. 10 shows the maximum error $\Delta\boldsymbol{\psi}_2$ of the rotor flux vector for all combinations of $\hat{J}_1$ and f_2 of the machine in dependency of the simulation time step *ts*.

The classic transient simulation with zero rotor flux linkage starting condition takes 336 simulation time steps to converge to an error of <5% and 600 time steps to an error of <1% in every combination. In contrast, much less simulation time steps are necessary to reach steady state for the coupled simulation. Less than 5% of error is reached after 136 simulation time steps and <1% error is reached after 368 time steps. For the modelled machine, the coupling of numerical and analytical simulation allows to reduce the simulation effort for the transient build-up of the rotor flux linkage by ∼50%.

The build-up of the rotor flux linkage is dependent on the rotor time constant T_2. Hence, the coupling of analytical and numerical models is more beneficial for IM with larger values of T_2. The rotor time constant T_2 is dependent on the rotor inductance L_2 and the rotor resistance R_2:

$$T_2 = \frac{L_2}{R_2}. \tag{17}$$

Larger machines with larger values of L_2 and machines with high efficiency, i.e. small values of R_2, have larger rotor time constants. The machine which is exemplary simulated here has a mechanical peak power of 40 kW and an aluminium squirrel cage. For mobile traction application requiring more power, higher efficiency and

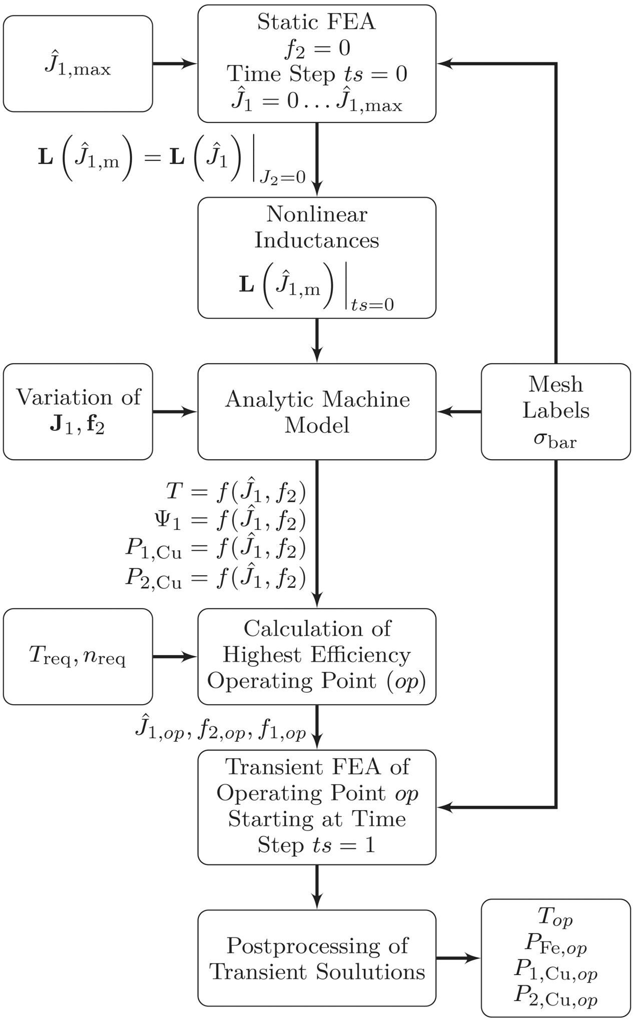

Fig. 11 *Scheme for hybrid simulation model finding the loss minimal operating point for a requested torque T speed n combination. Prediction of the starting value of rotor flux and transient FEA simulation of the T – n operating point*

higher power density, copper rotor cages are favourable. For those machines, the presented combination of analytical formulas and numerical simulations is even more beneficial in terms of simulation effort than for the exemplary machine. Considering larger drives, the effect of reducing simulation time becomes even more advantageous. For a machine in the 5 MW power range, e.g. for use in wind turbines, the rotor time constant is several seconds. Hence, for such large IM drives, the hybrid simulation model can drastically reduce the necessary simulation time to reach steady state.

3.3 Calculation of a single loss minimal torque–speed operating point

This second hybrid simulation scheme (Fig. 11) is a modification of the first simulation scheme (Fig. 7).

As in the first simulation scheme, no-load static FEA simulations in different saturation states k are conducted. From these simulations, the inductance matrices $\boldsymbol{L}(k)$ are extracted. Instead of analytically solving just one combination of stator current density $\hat{J}_1$ and rotor frequency f_2, the procedure from Section 3.2 is applied to a set of various operating points in terms of $\hat{J}_1 - f_2$. A grid with $\hat{J}_1$ on the first axis and f_2 on the second axis is formed. For this grid, $\hat{J}_1$ and f_2 are varied in equidistant steps, resulting in the tensors $\boldsymbol{J}_1$ and $\boldsymbol{f}_2$. For each of the combinations from $\boldsymbol{J}_1$ and $\boldsymbol{f}_2$, the torque T, the flux linkage $\boldsymbol{\psi}_1$ and the Ohmic losses in stator $P_{1,\mathrm{Cu}}$ and rotor $P_{2,\mathrm{Cu}}$ are solved by means of analytical formulation and interpolation of the saturation state (8)–(15). The saturation state is determined by solving (12) which results in the equivalent no-load current I_0 (13). The equivalent no-load current I_0 is used to numerically interpolate the rotor flux linkage, i.e. interpolating $\boldsymbol{\psi}_2$ from (10) according to (18):

$$\boldsymbol{\psi}_2\left(\hat{J}_1, f_2\right) = \boldsymbol{\psi}_2\left(J_1(k) = I_0(J_1, f_2)\frac{\sqrt{2}}{A_{\mathrm{s},1}}\right). \tag{18}$$

$$T = p \times \boldsymbol{\psi}_2^{\mathrm{T}} \times \boldsymbol{I}_2 \tag{19}$$

From the rotor flux linkage vector $\boldsymbol{\psi}_2$ and the rotor current vector, the torque T is calculated by means of (19). The Ohmic losses in the stator winding $P_{1,\mathrm{Cu}}$ and the rotor cage $P_{2,\mathrm{Cu}}$ are calculated according to (20) and (21). Thus, the Ohmic losses are calculated over the grid of $\boldsymbol{J}_1$ and $\boldsymbol{f}_2$. The Ohmic losses are used to find the lowest Ohmic loss operating point for a requested torque–speed operating point $(T_{\mathrm{req}}, n_{\mathrm{req}})$.

$$P_{1,\mathrm{Cu}}(I_1) = R_1 \times \boldsymbol{I}_1^{\mathrm{T}} \times \boldsymbol{I}_1 \tag{20}$$

$$P_{2,\mathrm{Cu}}(I_1, f_2) = R_{2,\mathrm{bar}} \times \boldsymbol{I}_2^{\mathrm{T}}(I_1, f_2) \times \boldsymbol{I}_2(I_1, f_2) \tag{21}$$

When finding the minimal Ohmic losses, the maximum stator voltage limitation $U_{1,\max}$ and the maximum stator current limitation $I_{1,\max}$ are taken into account. The loss minimisation formulation is given in (22):

$$\begin{aligned} &\min_{I_1, f_2} \left(P_{1,\mathrm{Cu}}(I_1, f_1) + P_{2,\mathrm{Cu}}(I_1, f_2)\right),\\ &\mathrm{s.t.}: T(I_1, f_2) = T_{\mathrm{req}},\\ &n(I_1, f_2) = n_{\mathrm{req}},\\ &U_1(I_1, f_2) \le U_{1,\max},\\ &I_1(f_2) \le I_{1,\max}\,. \end{aligned} \tag{22}$$

Solving (22) yields the current $I_1(T_{\mathrm{req}}, n_{\mathrm{req}})$ and the frequency $f_2(T_{\mathrm{req}}, n_{\mathrm{req}})$. From $I_1(T_{\mathrm{req}}, n_{\mathrm{req}})$, the current density in the stator slots $\hat{J}_1(T_{\mathrm{req}}, n_{\mathrm{req}})$ is calculated and a transient FEA simulation with the excitation $\hat{J}_1$ and f_2 is conducted using the first simulation scheme (Fig. 7). After simulating several transient time steps, the iron and Ohmic losses are calculated in the post processing. The iron losses are calculated using the transient iron loss formulation from [10]. The Ohmic losses in the rotor are calculated in every element i to take the local distribution of the Ohmic losses in the rotor bars into account.

Due to skin and proximity effect, the stator Ohmic losses are frequency dependent. The skin and proximity effect in the stator winding are calculated according to [11] and a frequency-dependent factor is applied to the Ohmic losses in the stator. In the following section, this loss simulation scheme is exemplary applied to find the influence of the slot opening shapes on the machine losses and the machines maximum torque.

4 Influence of stator and rotor slot opening shapes

The stator slot opening $w_{\mathrm{s},1}$ and rotor slot opening $w_{\mathrm{s},2}$ influence the magnetic circuit in various ways. Slotting in stator and rotor leads to an unevenly distributed magnetic flux density in the air gap. Thus, the coupling magnetic flux is decreased by slotting. This decrease of magnetic coupling can be described by a virtual increase of the air gap length from δ to δ' using Carter's factor k_{c} (23). The Carter factor is calculated using the slot pitch τ_{s}, the width of the slot opening w_{s} and the auxiliary number γ (24). The auxiliary number γ can be estimated to (25) for assuming infinitely deep slots and $\mu_{\mathrm{r}} \to \infty$.

$$\delta' = k_{\mathrm{c}} \cdot \delta \tag{23}$$

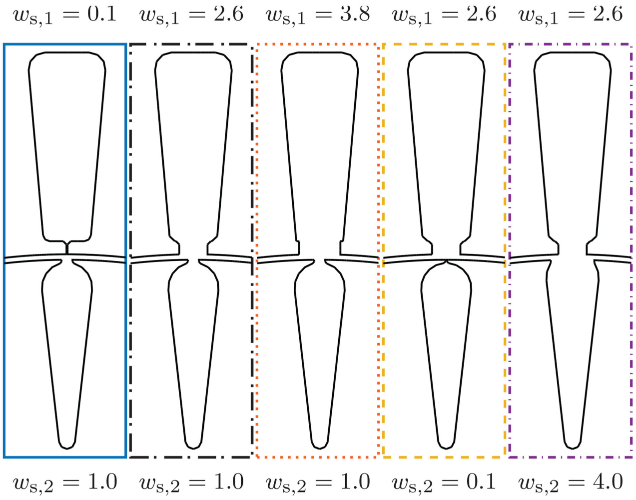

Fig. 12 *Stator and rotor slot openings (all slot opening dimensions $w_{s,1}$ and $w_{s,2}$ in mm)*

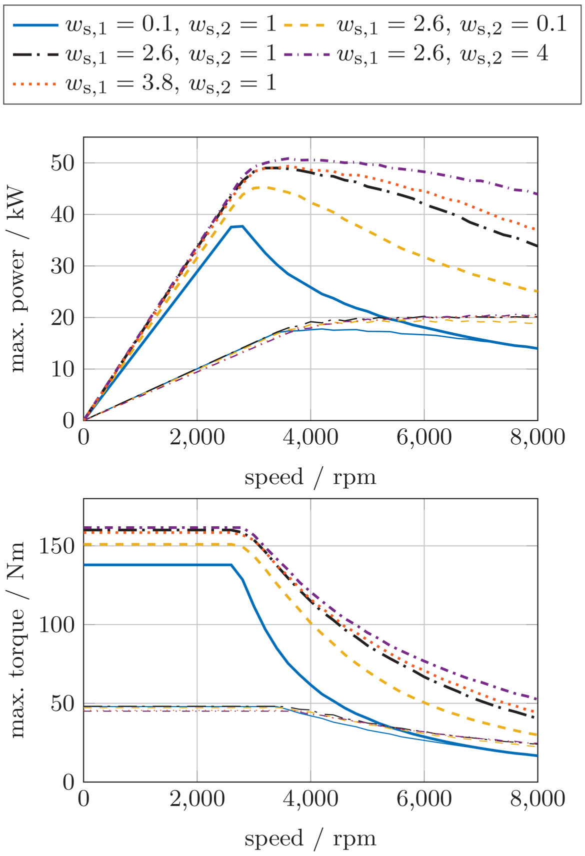

Fig. 13 *Influence of slot openings on maximum torque and power at $I_1 \leq 400$ A (thick lines) and $I_1 \leq 150$ A (thin lines). $w_{s,1}$ and $w_{s,2}$ in mm*

$$k_c = \frac{\tau_s}{\tau_s - \gamma w_s} \tag{24}$$

$$\gamma = \frac{1}{1 + 5(\delta/w_s)} \tag{25}$$

A smaller slot opening leads to an improved coupling of stator and rotor conductors which is described by a smaller value of the Carter factor k_c (24). However, smaller slot openings also lead to increased stray flux through the teeth tips. The third effect is that the design of the slot openings influences the harmonics in the air gap. The harmonics of the air gap field are partly damped by harmonic rotor currents which lead to additional Ohmic losses in the rotor. In the following, these various effects are analysed using FEA simulations according to the simulation scheme from Fig. 11.

The maximum torque characteristic in dependency of speed is derived by applying different values of T_{req} and n_{req} to the hybrid simulation scheme. The voltage and current limitation of $U_{\max} = 92$ V and $I_{\max} = 400$ A are regarded. Five of the simulated combinations of $w_{s,1}$ and $w_{s,2}$ are shown in Fig. 12. For those five combinations, the maximum torque and maximum mechanical power are calculated in dependency of the machine speed using the simulation approach shown in Fig. 11. The maximum torque and maximum power curves are plotted in Fig. 13. The voltage limitation is $U_1 \leq 92$ V (linked). The stator current limitation is $I_1 \leq 400$ A (thick lines). The thin lines represent the maximum torque at low load, i.e. at a lower stator current limit of $I_1 \leq 150$ A.

At lower maximum stator currents, the maximum mechanical power is lower. However, at lower maximum stator currents, the speed at which the maximum power can be provided increases. At $w_{s,1} = 2.6$ mm and $w_{s,2} = 1$ mm, the maximum power is delivered at $n = 3300$ rpm (400 A). At a current limit of 150 A for all combinations of w_s, except for ($w_{s,1} = 0.1$ mm and $w_{s,2} = 1$ mm), the maximum power is delivered at maximum speed $n = 8000$ rpm.

Fig. 14 shows the local distribution of the effective bar current density. The effective bar current density is cut at the coordinate $y = 0$. The values of the effective bar currents at these cut positions are plotted in Fig. 15. The minimum value of current density of $J_2 = 11.21\ \text{A/mm}^2$ occurs at the deepest position in the bar. Towards the surface of the rotor, the effective current density increases monotonic. At the most outer position of the bar, a current density of $J_2 = 16.92\ \text{A/mm}^2$ is simulated. Hence, for the precise calculation of the Ohmic losses in the rotor, the current distribution inside the bars has to be incorporated. Two maximum torque operating points are analysed in detail: maximum torque below base speed and maximum torque at maximum speed.

In the FEA simulation, the Ohmic losses in the rotor $P_{\text{Cu},2}$ are evaluated in every element i of the rotor bars using the element area A_i, the current density in the element $J_{2,i}$, the specific electric conductivity σ_{bar} and the length of the rotor bars l_{bar}:

$$P_{\text{Cu},2} = \sum_{i=1} (J_{2,i} A_i)^2 \cdot \frac{l_{\text{bar}}}{\sigma_{\text{bar}} A_i}. \tag{26}$$

The Ohmic losses in the rotor of the machine are calculated from a full rotor period from transient FEA simulations. In each element of the rotor bar labels, the fundamental component of the current density is determined by a Fourier frequency transformation. The Ohmic loss $P_{2,\text{Cu},1}$ in the rotor from the fundamental rotor current component is calculated according to (27) using the fundamental local current density $J_{2,i,1}$ in every bar element i.

$$P_{\text{Cu},2,1} = \sum_{i=1} (J_{2,i,1} A_i)^2 \cdot \frac{l_{\text{bar}}}{\sigma_{\text{bar}} A_i} \tag{27}$$

The influence of increased Ohmic losses in the rotor from higher harmonic amplitudes is analysed by dividing $P_{2,\text{Cu}}$ and $P_{2,\text{Cu},1}$, resulting in the Ohmic loss increase factor $k_{\text{Cu},2}$:

$$k_{\text{Cu},2} = \frac{P_{2,\text{Cu}}}{P_{2,\text{Cu},1}}. \tag{28}$$

Figs. 16*a* and *c* show the rotor Ohmic loss increase factor $k_{\text{Cu},2}$ in dependency of the slot openings $w_{s,1}$ and $w_{s,2}$. With larger slot openings w_s, the Ohmic losses in the rotor increase due to harmonic currents. This effect is stronger at maximum speed $n_{\max}$ than at base speed n_c. The Ohmic losses increase at n_c between 5.0 and 11.1%, whereas at $n_{\max}$, the increase is between 11.8 and 42%. At n_c, the Ohmic loss increase from harmonics caused by $w_{s,1}$ and $w_{s,2}$ is comparably small: from 5.0 to 9.0% for $w_{s,1}$ and from 7.3 to 11.1% for $w_{s,2}$. At maximum speed, the influence of $w_{s,1}$ and $w_{s,2}$ on $k_{\text{Cu},2}$ is quite different: $k_{\text{Cu},2}$ increases with $w_{s,1}$ stronger for smaller slot opening values, whereas it increases less strongly with $w_{s,2}$. At larger slot openings, the increase of $k_{\text{Cu},2}$ due to $w_{s,1}$ increases only

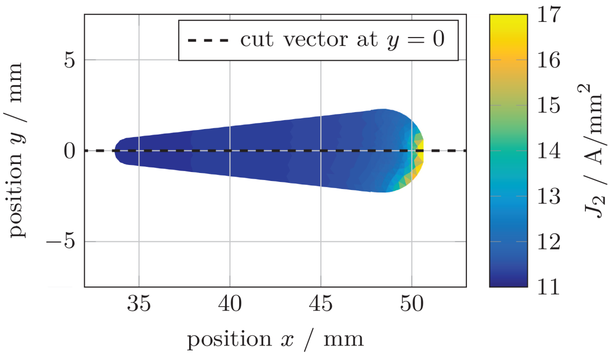

Fig. 14 *Simulated effective local rotor bar current density at* $\hat{J}_1 = 10\,\mathrm{A/mm^2}$*,* $f_2 = 5\,\mathrm{Hz}$ *and* $f_1 = 80\,\mathrm{Hz}$

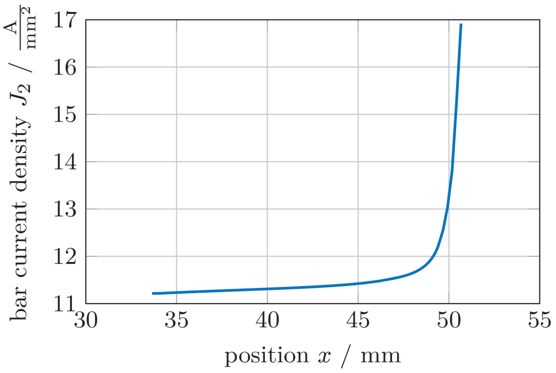

Fig. 15 *Simulated effective local rotor bar current density at* $\hat{J}_1 = 10\,\mathrm{A/mm^2}$*,* $f_2 = 5\,\mathrm{Hz}$ *and* $f_1 = 80\,\mathrm{Hz}$ *(cut through middle of bar, i.e.* $y = 0$*)*

slightly, whereas it increases strongly with $w_{\mathrm{s},2}$. At larger rotor slot openings, more conductive bar material is close to the rotor surface (Fig. 12). The harmonic rotor currents are concentrated to the rotor surface due to their high frequency. Having more conductive bar material close to the surface results in a smaller effective bar resistance for the rotor harmonic currents. The smaller effective resistance leads to higher values of the harmonic rotor currents and thus to increased Ohmic losses. Combining bar materials with different values of electric conductivity, such as copper and aluminium, could decrease this effect. A method for producing squirrel cages with combined bar materials is given in [12, 13].

The maximum torque at base speed n_c and at maximum speed n_max is plotted in Figs. 16*b* and *d*. At base speed, the maximum torque with a stator slot opening of $w_{\mathrm{s},1} = 0.1\,\mathrm{mm}$ is 137.7 Nm, 13.6% lower than the maximum torque at $w_{\mathrm{s},1} = 2.6\,\mathrm{mm}$. At the maximum speed and $w_{\mathrm{s},1} = 0.1\,\mathrm{mm}$, the maximum torque is 16.5 Nm, 62.6% less than at $w_{\mathrm{s},1} = 3.8\,\mathrm{mm}$.

The influence of $w_{\mathrm{s},2}$ on the maximum torque is smaller than the influence of $w_{\mathrm{s},1}$. The maximum torque at base speed varies between 150.4 Nm at $w_{\mathrm{s},2} = 0.1\,\mathrm{mm}$ and 161.3 Nm at $w_{\mathrm{s},2} = 3.0\,\mathrm{mm}$. At maximum speed, the maximum torque ranges between 29.9 Nm at $w_{\mathrm{s},2} = 0.1$ mm and 51.8 Nm at $w_{\mathrm{s},2} = 4$ mm.

The influence of the dimensions of the stator and rotor slot openings on the machine operating behaviour is summarised in Table 1. Smaller slot openings lead to larger stray inductances and thus to increased stray flux. When the machine is operated at the voltage limit, i.e. at high speed and medium to high torque, more voltage drops at the stray inductances. The maximum power at the voltage limit is therefore reduced for machines with small slot openings. For machines with less stray flux, the region where high-power values can be reached increases in terms of speed.

5 Conclusions

Two variants of a hybrid FEA simulation model for the simulation of IM as VSD in traction applications have been presented.

The first variant anticipates the steady state of the flux linkages to cut short the transient build-up of the rotor flux in non-linear transient FEA simulation. From a non-linear static FEA simulation with the stator current as the only excitation, the entire inductance matrices are extracted. The steady-state rotor currents are anticipated from the extracted matrices and analytic formulae. The steady-state rotor currents are used as additional excitation for a static simulation to pre-calculate the steady-state magnetic vector potential solution. For the studied traction drive with a peak power of 40 kW, the anticipation of the steady-state rotor flux linkage reduces the computational effort by ∼50%. For larger machines, i.e. machines with larger rotor time constant, higher savings in computational effort are expected. However, for simulating an operating point in terms of machine torque and machine speed, the corresponding excitations in terms of stator current and the frequency of the rotor currents have to be known.

The second presented variant of the hybrid FEA model has removed the requirement of knowing the operating point in terms of stator current and rotor frequency. The Ohmic loss minimal operating point in terms of stator current and rotor frequency is calculated from the demanded torque and speed within the voltage and current boundaries.

The presented hybrid FEA model is exemplary applied to a small parameter study. The slot openings in stator and rotor slots are varied to find the influence on machine characteristics. The maximum torque characteristics of the specimen were calculated using the hybrid simulation scheme. Two operating points that are relevant specification points for traction drives are analysed in detail: Maximum torque at base speed and maximum torque at maximum speed. In those two operating points, the transient FEA was conducted. The influence of the slot openings on maximum torque and the influence on losses due to harmonics in the rotor currents were derived. Especially, large rotor slot openings lead to an increase in Ohmic losses in the rotor bars due to harmonics. However, larger slot openings are favourable since they lead to decreased leakage inductances and to higher torque values above base speed.

The hybrid models have proved to simulate the losses of IM operated as VSD with reduced computational effort compared with full transient FEA formulations. The hybrid simulation model allows to specifically simulate machines in the operating points that are defined by the customer of such drives.

For future IM loss simulation tasks, the models can either reduce the simulation effort for simulation of single machines or increase the number of simulated design variants and therefore improve machine design cycles.

The model, which is designed for loss modelling, can be used in the future to provide lumped parameters for IM control design previous to prototyping stage, such as proposed by [14], for permanent magnet synchronous machines.

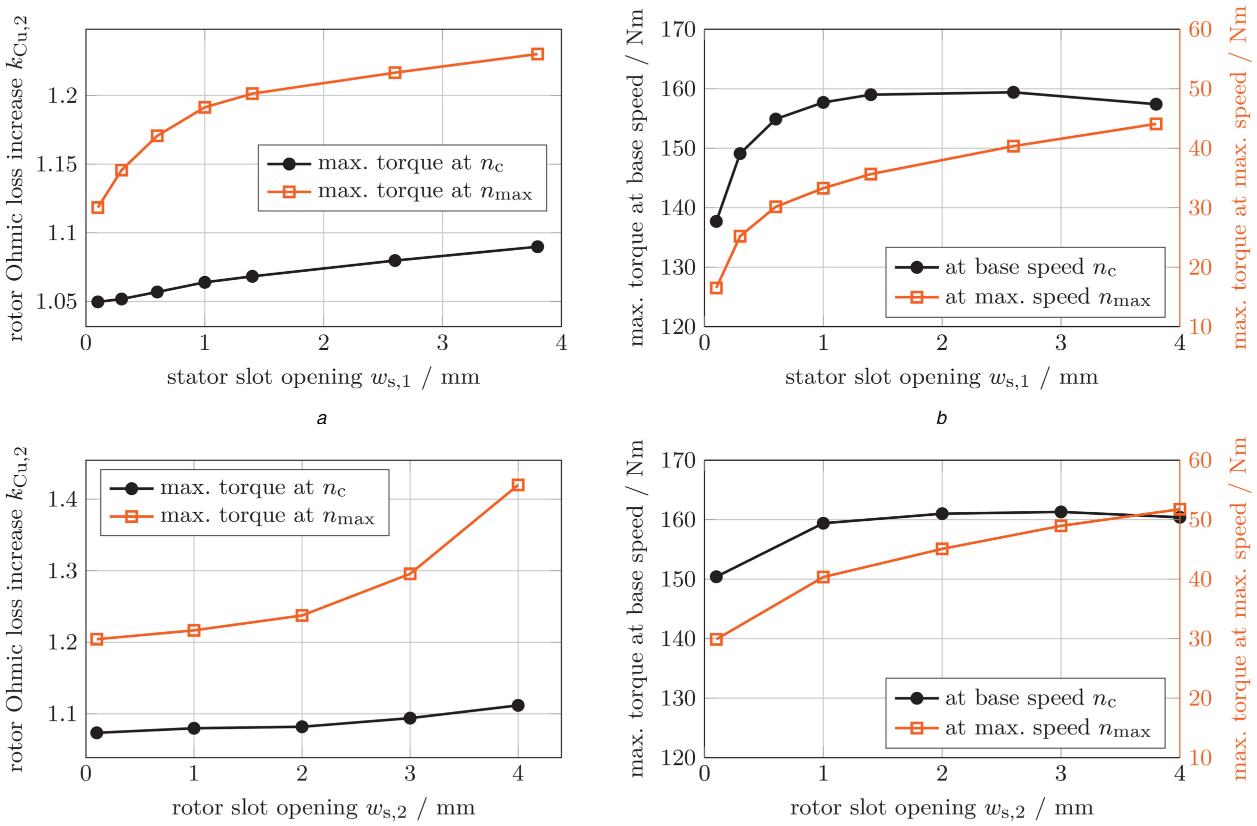

a *b*

c *d*

Fig. 16 *Influence of slot openings on Ohmic rotor losses and maximum torque at base speed and maximum speed*
(a) Loss increase rotor versus $w_{s,1}$, ***(b)*** Maximum torque versus $w_{s,1}$, ***(c)*** Loss increase rotor versus $w_{s,2}$, ***(d)*** Maximum torque versus $w_{s,2}$

Table 1 Influence of slot openings on the characteristics of IM

Slot opening	Low load	High load	
		Low speed	High speed
↓	currents ↓, efficiency ↑	currents ↑, max torque ↓	max torque ↓↓, harmonics I_2 ↓
↑	currents ↑, efficiency ↓	currents ↓, max torque ↑	max torque ↑, harmonics I_2 ↑

6 References

[1] Boldea, I., Tutelea, L.N., Parsa, L., *et al.*: 'Automotive electric propulsion systems with reduced or no permanent magnets: an overview', *IEEE Trans. Ind. Electron.*, 2014, **61**, (10), pp. 5696–5711

[2] Zhu, Z.Q., Chan, C.C.: 'Electrical machine topologies and technologies for electric, hybrid, and fuel cell vehicles'. Proc. of the 2008 IEEE Vehicle Power and Propulsion Conf., 2008

[3] Yang, Z., Shang, F., Brown, I.P., *et al.*: 'Comparative study of interior permanent magnet, induction, and switched reluctance motor drives for EV and HEV applications', *IEEE Trans Transport Electrific*, 2015, **1**, (3), pp. 245–254

[4] Oberretl, K.: 'Losses, torques and magnetic noise in induction motors with static converter supply, taking multiple armature reaction and slot openings into account', *IET Power Appl.*, 2007, **1**, (4), pp. 517–531

[5] Zhu, Z.Q., Howe, D.: 'Instantaneous magnetic field distribution in brushless permanent magnet DC motors. III. Effect of stator slotting', *IEEE Trans. Magn.*, 1993, **29**, (1), pp. 143–151

[6] Dorrell, D.G., Popescu, M., Evans, L., *et al.*: 'Modern electrical machine analysis and design techniques applied to hybrid vehicle drive machines'. 2010 IEEE Int. Symp. on Industrial Electronics, 2010, pp. 3728–3733

[7] von Pfingsten, G., Steentjes, S., Hameyer, K.: 'Operating point resolved loss calculation approach in saturated induction machines', *IEEE Trans. Ind. Electron.*, 2017, **64**, (3), pp. 2538–2546

[8] von Pfingsten, G., Steentjes, S., Hameyer, K.: 'Transient approach to model operating point dependent losses in saturated induction machines'. 2016 XXII Int. Conf. on Electrical Machines, 2016, pp. 626–632

[9] Henrotte, F., Heidt, J., Hameyer, K.: 'The mathematics of lumped parameter identification in electrical machines'. 2008 IET 7th Int. Conf. on Computation in Electromagnetics, 2008, pp. 28–29

[10] Lin, D., Zhou, P., Fu, W.N., *et al.*: 'A dynamic core loss model for soft ferromagnetic and power ferrite materials in transient finite element analysis', *IEEE Trans. Magn.*, 2004, **40**, (2), pp. 1318–1321

[11] Carstensen, C.: 'Eddy currents in windings of switched reluctance machines'. PhD thesis, RWTH Aachen University, Aachen, Germany, 2008

[12] Brandes, J., Inventor; Siemens, assignee: 'Squirrel-cage rotor for an asynchronous machine'. DE Patent 4308683 A1, 1994

[13] Wöhner, N., inventor; Siemens, assignee: 'Cage rotor for asynchronous machine, has rotor lamination stack comprising electrical sheet, and groove inserts lying at groove edge of grooves and reducing groove cross section surface to another groove cross section surface'. DE Patent 102009051488 A1, 2011

[14] Herold, T., Franck, D., Lange, E., *et al.*: 'Extension of a *d–q* model of a permanent magnet excited synchronous machine by including saturation, cross-coupling and slotting effects'. 2011 IEEE Int. Electric Machines Drives Conf., 2011, pp. 1363–1367